# Blind Image Deconvolution Based on Adaptive Euler's Elastica Regularization

Xiuzheng Song, Jun Zhang, Jingjing Lu, Sanping Rao

***Abstract*—Blind image deconvolution has garnered significant attention in the realm of image processing. Among existing blind deconvolution models, the adaptive weighted total variation-based model can better recover local image features. However, this model may give rise to undesirable staircase effects. In contrast, when considering non-blind deconvolution, a model that uses adaptive Euler's elastica (AEE) regularization can reduce the appearance of staircase effects and better maintain image local features. Inspired by the successful application of the AEE regularization in non-blind deconvolution, we propose an AEE model for blind image deconvolution. This novel model can preserve image features in smooth regions and restore local characteristics of the image. In addition, an efficient alternating direction method of multipliers is designed to address this non-convex model. Experimental results illustrate the superiority of the proposed method compared with other related blind deconvolution methods.**

***Index Terms*—Blind deconvolution; Euler's elastica regularization; Adaptive weighted matrix; Alternating direction method of multipliers (ADMM).**

## I. Introduction

DEGRADATION of image quality occurs during image formation, transmission, and recording due to imperfections in the imaging system, transmission media, and equipment. Mathematically, the process of image degradation could be expressed as

$$f = k * u + n. \tag{1}$$

In this equation, $u$ stands for the original image, $f$ denotes the corrupted image, $k$ represents the point spread function (PSF), also known as the blur kernel, and $n$ signifies additive Gaussian noise. Depending on whether the blur kernel is known during the degradation process, image deconvolution techniques can be classified into two categories: non-blind and blind deconvolution. Early work on image deconvolution centered around non-blind deconvolution where the blur kernel is known, and there has been much research on non-blind deconvolution [1]–[6]. Nevertheless, in most practical engineering applications, obtaining accurate information about the blur kernel is often not feasible. As a result, blind deconvolution has received increasing attention from researchers in recent years [7]–[9]. To address this challenging problem, existing methods can be briefly divided into two categories. The first method is based on the selection of saliency edge [10]–[12], and the second is based on prior information. [13]–[19]. It should be noted that the edge-based approach does not apply to images with minimal texture structure, such as the face images. If the image edges are not selected appropriately, the accuracy of the blur kernel estimation will be reduced, leading to unsuccessful deconvolution results. Conversely, statistical priors for blur kernels and real images have been widely explored in recent years, such as heavy-tailed distribution of gradients [13], $L_1 - L_2$ regularization prior [14], $L_0$ prior [15], patch-based prior [16], dark channel prior [17], low-rank prior [18], local maximum gradient prior [19], etc.

As an effective prior, the total variation (TV) regularization was first used by Chan et al. for blind image deconvolution [20]. The corresponding minimization problem can be represented as

$$\min_{u,k} \|\nabla u\|_1 + \beta\|\nabla k\|_1 + \frac{\lambda}{2}\|k * u - f\|_2^2, \tag{2}$$

where the first and second terms are the regularization terms of the clear image $u$ and the blur kernel $k$, respectively, and the last is a data fidelity term. $\nabla$ stands for the gradient operator, and $\beta$ is a regularization parameter. The anisotropic diffusion property of TV regularization can be leveraged to handle image edges effectively. However, solving the model is a challenging task due to its nonlinear and non-differentiability nature. To deal with this problem, various algorithms have been developed [21]–[23]. Additionally, although the traditional TV model does a good job of preserving the image edges, it is not as effective in dealing with local features of images. Therefore, in [24], a blind deconvolution approach was introduced, using adaptive weighted TV regularization (called AWTV-BD). Notably, they combine the gradient operator of the image with an adaptive weighted matrix. Specifically, the orientation of the gradient operator is rotated due to the presence of this matrix so that it tends to bigger weight and thus better describes the local features in image. The AWTV-BD model can be described as follows:

$$\min_{u,k} \|\mathbf{T}\nabla u\|_1 + \beta\|\nabla k\|_1 + \frac{\lambda}{2}\|k * u - f\|_2^2, \tag{3}$$

where $\mathbf{T}$ is the adaptive weighted matrix. Specific form is

$$\begin{aligned}\mathbf{T}(i,j) &= \begin{bmatrix} t_1(i,j) & 0 \\ 0 & t_2(i,j) \end{bmatrix} \\ &= \begin{bmatrix} \frac{1}{1+\iota|G_\delta(i,j)*\nabla_x f(i,j)|} & 0 \\ 0 & \frac{1}{1+\iota|G_\delta(i,j)*\nabla_y f(i,j)|} \end{bmatrix}.\end{aligned} \tag{4}$$

Manuscript received July 13, 2023; revised October 24, 2023.

This work was partly supported by the Natural Science Foundation of Jiangxi Province (20232BAB201017), and the Science Foundation for Post Doctorate of China (2020M672484).

Xiuzheng Song is a postgraduate student of College of Science, Nanchang Institute of Technology, Nanchang 330099, Jiangxi, China. (e-mail: xiuzhengsong0616@163.com).

Jun Zhang is an associate professor of College of Science, Nanchang Institute of Technology, Nanchang 330099, Jiangxi, China. (corresponding author, e-mail: junzhang0805@126.com).

Jingjing Lu is a postgraduate student of Jiangxi Province Key Laboratory of Water Information Cooperative Sensing and Intelligent Processing, Nanchang Institute of Technology, Nanchang 330099, Jiangxi, China. (e-mail: jingjinglu0924@163.com).

Sanping Rao is an associate professor of College of Science, Nanchang Institute of Technology, Nanchang 330099, Jiangxi, China. (e-mail: raosanping81@sina.com).

Here, $G_\delta(\cdot)$ represents a Gaussian convolution kernel, $\nabla_x f$ and $\nabla_y f$ refer to the horizontal and vertical gradients of $f$, respectively, $\delta$ and $\iota$ serve as two adjustable parameters. In recent years, adaptive techniques have experienced widespread adoption in diverse image processing problems [25]–[29].

Although the AWTV-BD model can effectively preserve the local features of the image while maintaining the image edges, the deconvoluted image tends to have staircase effects in flat areas. In the last two decades, many higher-order models have been proposed to overcome the staircase effects and better recover the image features in the smoothed regions. [30]–[34]. Particularly, within the domain of non-blind image deconvolution, Yang et al. [29] presented an adaptive Euler's elastica (AEE) model, which can be formulated as follows:

$$\min_u \sum_{i,j} g(\kappa(u_{i,j}))|\mathbf{T}\nabla u_{i,j}| + \frac{\lambda}{2}\|u-f\|_2^2. \tag{5}$$

Here, $g(\kappa(u))$ is a specific function as

$$g(\kappa(u)) = 1 + \alpha|\kappa(u)|, \tag{6}$$

where $\kappa(u) = \nabla \cdot \left(\frac{\nabla u}{|\nabla u|}\right)$ denotes the curvature of the level curve $u(x,y) = c$. This model can achieve faster attenuation of the high-frequency components of the image, reducing the staircase effects and resulting in a more naturally restored image. As the model is non-convex, the associated algorithm converges to a locally optimal solution. Especially, when $\iota = 0$, $\mathbf{T}(i,j)$ becomes the identity matrix. In this case, the model (5) is related to Euler's elastica model [35], [36].

Inspired by the successful application of the AEE regularization in non-blind deconvolution, we extend its usage to blind deconvolution of images. The main contributions of this paper are threefold:

- A new blind image deconvolution model is proposed based on an adaptive Euler's elastica regularization. The adaptive weighted matrix allows the model to handle the local structures of the image better. To solve this non-convex and non-smooth model, we propose an efficient ADMM.
- Extensive experimental results concerning blind image deconvolution have been furnished to showcase the cutting-edge performance of the proposed method.

The rest of this paper is organized as follows. In section 2, we propose a novel model for blind image deconvolution that utilizes an adaptive Euler's elastica regularization. The ADMM for solving the proposed model is presented in Section 3. In Section 4, extensive experiments are conducted to verify the efficiency of our approach compared with the state-of-the-art methods. Finally, some conclusions are given in Section 5.

## II. The Proposed Model

This section focuses on constructing a novel blind deconvolution model for images. The TV-based blind deconvolution model (2) is isotropic due to the use of the same weight for the sub-variables in the gradient operator. Therefore, it cannot effectively deal with the local features of images. To overcome this drawback, in [24], the authors proposed the AWTV-BD model (3) for blind image deconvolution. This model is able to spread along the tangential direction of local features, recovering the local structure of the image more effectively. Nevertheless, there are staircase effects in the restored images using the AWTV-BD model. For non-blind deconvolution, Yang et al. [29] proposed an AEE-based model. Specifically, they used the curvature of the image as a prior for the model, which can alleviate the staircase effects to a certain extent and maintain the image features in smooth regions. In addition, the adaptive weighted matrix can enhance the preservation of local image features. Inspired by the AEE regularization strategy, we propose a blind image deconvolution model based on the AEE regularization:

$$\min_{u,k} \sum_{i,j} g(\kappa(u_{i,j}))|\mathbf{T}\nabla u_{i,j}| + \beta\|\nabla k\|_1 + \frac{\lambda}{2}\|k*u-f\|_2^2. \tag{7}$$

Here, the regularization parameters $\beta$ and $\lambda$ balance the data fidelity and regularization terms. $g(\kappa(u))$ is defined as shown in equation (6). It is worth noting that when $\alpha = 0$, the model reduces to the AWTV-BD model.

## III. Algorithm

This section proposes an efficient ADMM [24], [34] for obtaining optimal solutions to the above non-convex and non-smooth optimization problem. First, we transform the proposed model (7) into the following constrained optimization problem.

$$\begin{aligned} &\min_{u,k,\mathbf{p},\mathbf{q},\mathbf{w}} \sum_{i,j} g(\kappa(u_{i,j}))|\mathbf{q}_{i,j}| + \beta\|\mathbf{w}\|_1 + \frac{\lambda}{2}\|k*u-f\|_2^2, \\ &\text{s.t.} \quad \mathbf{p} = \nabla u, \mathbf{q} = \mathbf{T}\mathbf{p}, \mathbf{w} = \nabla k. \end{aligned} \tag{8}$$

Then, the augmented Lagrangian function of the constrained optimization problem (8) is as follows:

$$\begin{aligned} \mathcal{L}(k,u,\mathbf{p},\mathbf{q},\mathbf{w};\boldsymbol{\lambda}_1,\boldsymbol{\lambda}_2,\boldsymbol{\lambda}_3) &= \sum_{i,j} g(\kappa(u_{i,j}^n))|\mathbf{q}_{i,j}| \\ &+ \beta\|\mathbf{w}\|_1 + \frac{\lambda}{2}\|Ku-f\|_2^2 + \frac{r_1}{2}\|\mathbf{p}-\nabla u-\boldsymbol{\lambda}_1\|_2^2 \\ &+ \frac{r_2}{2}\|\mathbf{q}-\mathbf{T}\mathbf{p}-\boldsymbol{\lambda}_2\|_2^2 + \frac{r_3}{2}\|\mathbf{w}-\nabla k-\boldsymbol{\lambda}_3\|_2^2, \end{aligned} \tag{9}$$

where $\boldsymbol{\lambda}_1$, $\boldsymbol{\lambda}_2$, $\boldsymbol{\lambda}_3$ are three Lagrangian multipliers, and $r_1$, $r_2$ and $r_3$ are three penalty parameters. $K$ denotes the blurring matrix. In applying ADMM, we need to minimize five subproblems with other variables fixed and update three Lagrangian multipliers at each iteration, that is

$$\begin{cases} k^{n+1} = \arg\min_k \mathcal{L}(k,u^n,\mathbf{p}^n,\mathbf{q}^n,\mathbf{w}^n;\boldsymbol{\lambda}_1^n,\boldsymbol{\lambda}_2^n,\boldsymbol{\lambda}_3^n), \\ u^{n+1} = \arg\min_u \mathcal{L}(k^{n+1},u,\mathbf{p}^n,\mathbf{q}^n,\mathbf{w}^n;\boldsymbol{\lambda}_1^n,\boldsymbol{\lambda}_2^n,\boldsymbol{\lambda}_3^n), \\ \mathbf{p}^{n+1} = \arg\min_{\mathbf{p}} \mathcal{L}(k^{n+1},u^{n+1},\mathbf{p},\mathbf{q}^n,\mathbf{w}^n;\boldsymbol{\lambda}_1^n,\boldsymbol{\lambda}_2^n,\boldsymbol{\lambda}_3^n), \\ \mathbf{q}^{n+1} = \arg\min_{\mathbf{q}} \mathcal{L}(k^{n+1},u^{n+1},\mathbf{p}^{n+1},\mathbf{q},\mathbf{w}^n;\boldsymbol{\lambda}_1^n,\boldsymbol{\lambda}_2^n,\boldsymbol{\lambda}_3^n), \\ \mathbf{w}^{n+1} = \arg\min_{\mathbf{w}} \mathcal{L}(k^{n+1},u^{n+1},\mathbf{p}^{n+1},\mathbf{q}^{n+1},\mathbf{w};\boldsymbol{\lambda}_1^n,\boldsymbol{\lambda}_2^n,\boldsymbol{\lambda}_3^n), \\ \boldsymbol{\lambda}_1^{n+1} = \boldsymbol{\lambda}_1^n + \nabla u^{n+1} - \mathbf{p}^{n+1}, \\ \boldsymbol{\lambda}_2^{n+1} = \boldsymbol{\lambda}_2^n + \mathbf{T}\mathbf{p}^{n+1} - \mathbf{q}^{n+1}, \\ \boldsymbol{\lambda}_3^{n+1} = \boldsymbol{\lambda}_3^n + \nabla k^{n+1} - \mathbf{w}^{n+1}. \end{cases} \tag{10}$$

The $k$-subproblem could be represented as

$$k^{n+1} = \arg\min_k \frac{\lambda}{2}\|U^n k-f\|_2^2 + \frac{r_3}{2}\|\mathbf{w}^n-\nabla k-\boldsymbol{\lambda}_3^n\|_2^2. \tag{11}$$

Here, $U$ refers to a block cycle matrix composed of the image $u$. In this paper, the periodic boundary condition is assumed.

Thus, we can obtain the solution by fast Fourier transform (FFT) as

$$k^{n+1} = F^{-1}\left[\frac{F\left(\lambda(U^n)^T f + r_3\nabla^T(\mathbf{w}^n - \boldsymbol{\lambda}_3^n)\right)}{F\left(\lambda(U^n)^T U^n + r_3\nabla^T\nabla\right)}\right], \quad (12)$$

in which $F$ and $F^{-1}$ respectively represent FFT and its inverse transformation, and $\nabla^T = -div$ signifies the adjoint of $\nabla$.

Similarly, the u-subproblem can be formulated as follows:

$$u^{n+1} = \arg\min_u \frac{\lambda}{2}\|K^{n+1}u - f\|_2^2 + \frac{r_1}{2}\|\mathbf{p}^n - \nabla u - \boldsymbol{\lambda}_1^n\|_2^2. \quad (13)$$

By using the FFT again, we get

$$u^{n+1} = F^{-1}\left[\frac{F\left(\lambda(K^{n+1})^T f + r_1\nabla^T(\mathbf{p}^n - \boldsymbol{\lambda}_1^n)\right)}{F\left(\lambda(K^{n+1})^T K^{n+1} + r_1\nabla^T\nabla\right)}\right]. \quad (14)$$

The p-subproblem can be articulated as

$$\begin{aligned}\mathbf{p}^{n+1} = \arg\min_{\mathbf{p}} &\frac{r_1}{2}\|\mathbf{p} - \nabla u^{n+1} - \boldsymbol{\lambda}_1^n\|_2^2 \\ &+ \frac{r_2}{2}\|\mathbf{q}^n - \mathbf{T}\mathbf{p} - \boldsymbol{\lambda}_2^n\|_2^2.\end{aligned} \quad (15)$$

According to its optimality condition, we derive the corresponding linear equation compiled as

$$\begin{aligned}&\begin{bmatrix} r_1 + r_2 t_1^2 & 0 \\ 0 & r_1 + r_2 t_2^2 \end{bmatrix}\begin{bmatrix} p_1^{n+1} \\ p_2^{n+1}\end{bmatrix} = \\ &\begin{bmatrix} r_1(\nabla_x u^{n+1} + \lambda_{11}^n) + r_2 t_1(q_1^n - \lambda_{21}^n) \\ r_1(\nabla_y u^{n+1} + \lambda_{12}^n) + r_2 t_2(q_2^n - \lambda_{22}^n)\end{bmatrix}.\end{aligned} \quad (16)$$

Thus, it is easy to get an explicit solution for $\mathbf{p}$ from equation (16) as

$$\begin{cases} p_1^{n+1} = \dfrac{r_1(\nabla_x u^{n+1} + \lambda_{11}^n) + r_2 t_1(q_1^n - \lambda_{21}^n)}{r_1 + r_2 t_1^2}, \\ p_2^{n+1} = \dfrac{r_1(\nabla_y u^{n+1} + \lambda_{12}^n) + r_2 t_2(q_2^n - \lambda_{22}^n)}{r_1 + r_2 t_2^2}. \end{cases} \quad (17)$$

The q-subproblem could be denoted as

$$\begin{aligned}\mathbf{q}^{n+1} = \arg\min_{\mathbf{q}} &\sum_{i,j} g(\kappa(u_{i,j}^n))|\mathbf{q}_{i,j}| \\ &+ \frac{r_2}{2}\|\mathbf{q} - \mathbf{T}\mathbf{p}^{n+1} - \boldsymbol{\lambda}_2^n\|_2^2.\end{aligned} \quad (18)$$

The soft-thresholding operator can provide a closed-form solution for this subproblem.

$$\begin{aligned}\mathbf{q}_{i,j}^{n+1} &= \text{soft}\left((\mathbf{T}\mathbf{p}^{n+1} + \boldsymbol{\lambda}_2^n)_{i,j}, \frac{g(\kappa(u_{i,j}^n))}{r_2}\right) \\ &= \max(|(\mathbf{T}\mathbf{p}^{n+1} + \boldsymbol{\lambda}_2^n)_{i,j}| - \frac{g(\kappa(u_{i,j}^n))}{r_2}, 0) \\ &\quad \cdot \text{sign}((\mathbf{T}\mathbf{p}^{n+1} + \boldsymbol{\lambda}_2^n)_{i,j}).\end{aligned} \quad (19)$$

The w-subproblem could be stated as

$$\mathbf{w}^{n+1} = \arg\min_{\mathbf{w}} \beta\|\mathbf{w}\|_1 + \frac{r_3}{2}\|\mathbf{w} - \nabla k^{n+1} - \boldsymbol{\lambda}_3^n\|_2^2. \quad (20)$$

In the same way, the solution to the w-subproblem can be given by the soft-thresholding operator

$$\mathbf{w}_{i,j}^{n+1} = \text{soft}\left((\nabla k^{n+1} + \boldsymbol{\lambda}_3^n)_{i,j}\ ,\ \frac{\beta}{r_3}\right). \quad (21)$$

It is essential to mention that the solution $(u, k)$ generated by the proposed model may not be unique. Therefore, to obtain the unique reasonable solution, we need to impose certain constraints on $k$ and $u$. As with the previous approaches [21], [24], the image intensities are of nonnegativity, and the estimated PSF is normalized. Specifically,

$$\int k^n(x,y)dxdy = 1, \quad (22)$$

and

$$u^n(x,y) = \begin{cases} u^n(x,y), & u^n(x,y) \geq 0, \\ 0, & \text{else.}\end{cases} \quad (23)$$

In particular, since the size of the support domain of the true PSF is unknown, we set the initial PSF size to be larger than the true PSF size and take the components outside the true PSF support domain as 0. There is bound to be some noise in the estimated PSF that affects the final deconvolution result. Therefore, we exploit dynamic threshold constraints during the iterative process to improve the PSF. Specifically, we utilize

$$k^n(x,y) = \begin{cases} k^n(x,y), & k^n(x,y) \geq \xi\max(k^n), \\ 0, & \text{else.}\end{cases} \quad (24)$$

Here, we denote the maximum value of the nth estimated PSF by $max(k^n)$. $\xi > 0$ is a minor number, and we experimentally set Xi=0.05.

Algorithm 3.1 summarizes the entire solution process for the presented model.

**Algorithm 3.1** ADMM to solve the problem (7)

1. Input and initialize: $u^0 = f, \mathbf{p}^0 = \boldsymbol{\lambda}_1^0 = \mathbf{q}^0 = \boldsymbol{\lambda}_2^0 = \mathbf{w}^0 = \boldsymbol{\lambda}_3^0 = \mathbf{0}$. Let $n := 0$.
2. $k^{n+1} = \arg\min_k \frac{\lambda}{2}\|U^n k - f\|_2^2 + \frac{r_3}{2}\|\mathbf{w}^n - \nabla k - \boldsymbol{\lambda}_3^n\|_2^2$,
3. Impose constraints on $k$.
4. $u^{n+1} = \arg\min_u \frac{\lambda}{2}\|K^{n+1}u - f\|_2^2 + \frac{r_1}{2}\|\mathbf{p}^n - \nabla u - \boldsymbol{\lambda}_1^n\|_2^2$.
5. Impose constraints on $u$.
6. Calculating $\mathbf{p}^{n+1}$ through (17).
7. Calculating $\mathbf{q}^{n+1}$ through (19).
8. Calculating $\mathbf{w}^{n+1}$ through (21).
9. Update $\boldsymbol{\lambda}_1^{n+1}$, $\boldsymbol{\lambda}_2^{n+1}$ and $\boldsymbol{\lambda}_3^{n+1}$
10. If the stopping condition is met, then stop. If not, increase $n$ by one and proceed to Step 2.

## IV. Numerical Experiments

In this section, we conduct experiments on natural and synthetic images and give related results for comparison with the EP-$L_0$RG model [37] and the AWTV-BD model [24]. Meanwhile, we refer to the newly proposed model as AEE-BD for simplicity of presentation. The experimental results demonstrate the validity and superiority of our proposed AEE-BD model.

All numerical experiments are performed in the MATLAB environment on a PC with a 2.50 GHz Intel(R) Core(TM) i5-12500 CPU and 16GB RAM. We scale the pixel values of all images to the interval [0,1]. To evaluate the quality of the blind deconvolution results, quantitatively, the performance of the algorithms is evaluated using three qualitative metrics, peak-signal-to-noise ratio (PSNR), improved signal-to-noise

ratio (ISNR), and structural similarity (SSIM). The specific definition of PSNR is

$$\text{PSNR} = 10\log_{10}\frac{1^2}{\frac{1}{MN}\sum_{i=1}^{M}\sum_{j=1}^{N}(u_{i,j}-I_{i,j})^2}, \quad (25)$$

where $I$ represents the original clear image and $u$ stands for the recovered image. N and M denote the width and length of the image, respectively. The ISNR is defined as

$$\text{ISNR} = 10\log_{10}\frac{\|f-I\|_2^2}{\|u-I\|_2^2}, \quad (26)$$

where $f$ is the degraded image. The definition of SSIM is as follows:

$$\text{SSIM} = \frac{(2\mu_I\mu_u + c_1)(2\sigma_{Iu} + c_2)}{({\mu_I}^2 + {\mu_u}^2 + c_1)({\sigma_I}^2 + {\sigma_u}^2 + c_2)}, \quad (27)$$

where $\mu_I$ and $\mu_u$ respectively stand for the mean values of images $I$ and $u$. The standard deviations of images $I$ and $u$ are denoted by $\sigma_I$ and $\sigma_u$, respectively, and their covariance is $\sigma_{Iu}$. The constants $c_1 > 0$ and $c_2 > 0$ are employed to prevent extremely small denominator values. In general, enhanced values of PSNR, ISNR, and SSIM mean an improved quality for the recovered image. An expression for the relative error of $u^n$ is given below:

$$R(u^n) = \frac{\| u^n - u^{n-1} \|_2}{\| u^{n-1} \|_2}. \quad (28)$$

When $R(u^n) < 10^{-4}$ or 500 iterations, the iteration terminates.

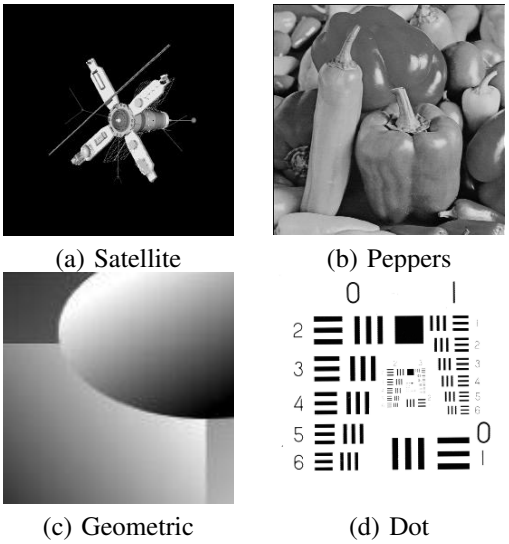

(a) Satellite (b) Peppers

(c) Geometric (d) Dot

**Fig. 1.** Test images.

Fig. 1 shows the Satellite (256 × 256), Peppers (256 × 256), Geometric (120 × 120), and Dot (256 × 256) as the four images tested in our experiments. We util the "fspecial" command in MATLAB to add different types of blur kernels to the image. Two types of blur kernels are shown in Fig. 2, linear motion blur with a length of 8 pixels and an orientation of 45 degrees and Gaussian blur with a size of 7x7 pixels and a variance of 25. And the size of the PSF is set to 101 × 101 pixels. Additionally, the Gaussian noise is added to the blurry image.

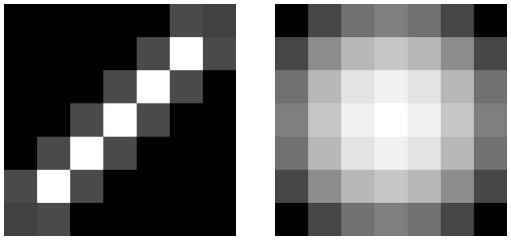

(a) linear motion (b) Gaussian

**Fig. 2.** Blur kernels for image degradation.

In our proposed model, there are a total of five parameters, namely $\lambda$, $\beta$, $\alpha$, $\iota$, and $\delta$. In general, the result of blind image deconvolution mainly depends on the regularization parameters $\lambda$, $\beta$, $\alpha$, the values of which affect the balance between the regularization and fidelity terms. Taking too little value for $\lambda$ will result in an overly smooth recovered image with lost image detail. In contrast, when $\lambda$ is set to a large value, there will be noise residue, resulting in a non-smooth recovered image. Therefore, the value of $\lambda$ should be chosen according to the structure of the image and the degree of degradation. In our experiments, the range of $\lambda$ value is set to $[3 \times 10^2, 1.5 \times 10^4]$. In particular, the optimal value of $\lambda$ becomes smaller as the noise level rises. $\beta$ represents the regularization parameter for $k$, influencing the extent of the PSF expansion. When large deviations in the PSF occur, it indicates that the value of $k$ was obtained too large. Instead, if the estimated support domain of the PSF was partially extended, it suggests that the value of $k$ was obtained too small. Hence, we assign $\beta \in [1 \times 10^{-2}, 1 \times 10^4]$. The parameter $\alpha > 0$ is to balance the curvature and surface area. To obtain satisfactory results for the blind deconvolution of images, it is essential to choose the optimal values for the three parameters mentioned above.

$\iota$ and $\delta$ are the parameters of the adaptive weighted matrix. Specifically, $\iota$ is used to control local adaptation, and $\delta$ is the standard deviation, which can be selected according to [25]. $r_1$, $r_2$, and $r_3$ are three penalty parameters that affect the convergence speed and stability of the algorithm. According to equation (17), (19), (21), they control the updating of **p**, **q**, **w**. Based on previous experience, we set $r_1 \in [1, 2\times10^3]$, $r_2 \in [1 \times 10^{-1}, 1.2 \times 10^3]$, and $r_3$ to be multiples of 5.

The two different blur kernels from Fig. 2 are respectively added to all the test images in Fig. 1, and the resulting blurred images are contaminated with additive Gaussian noise with a standard variance of 0.005. Especially, the numerical results of the blind deconvolution at low noise level 0.005 are given in Table I. It's evident that our approach consistently yields the highest PSNR values, and in the majority of cases, it also attains the highest SSIM values. It can also be seen that AEE-BD improves higher values in dealing with linear motion blur than with Gaussian blur compared to other methods. Therefore, AEE-BD is more suitable for removing linear motion blur.

The results of the different blind deconvolution methods on the two synthetic images are exhibited in Figs. 3 and 4, respectively. Specifically, each figure shows the recovered image, the recovered blur kernel, and the residual image $f - u$. As can be seen from Fig. 3, the recovered image of EP-L$_0$RG loses a lot of details in the edge part compared to the original image. Since both AWTV-BD and AEE-BD use

**TABLE I** Blind deconvolution numerical results in Gaussian noise of 0.005 standardized variance.

| Image | Blur type | Method | PSNR | ISNR | SSIM |
|---|---|---|---|---|---|
| Satellite | linear motion | EP-$L_0$RG | 31.97 | 6.05 | 0.953 |
| | | AWTV-BD | 33.26 | 7.54 | 0.956 |
| | | AEE-BD | **33.71** | **7.78** | **0.958** |
| | Gaussian | EP-$L_0$RG | 28.85 | 4.66 | 0.896 |
| | | AWTV-BD | 30.23 | 6.04 | 0.913 |
| | | AEE-BD | **30.45** | **6.26** | **0.922** |
| Peppers | linear motion | EP-$L_0$RG | 27.45 | 4.07 | 0.896 |
| | | AWTV-BD | 31.42 | 7.97 | 0.917 |
| | | AEE-BD | **31.70** | **8.25** | **0.919** |
| | Gaussian | EP-$L_0$RG | 26.33 | 3.85 | 0.820 |
| | | AWTV-BD | 31.00 | 8.52 | 0.898 |
| | | AEE-BD | **31.12** | **8.64** | **0.899** |
| Geometric | linear motion | EP-$L_0$RG | 32.90 | 5.59 | 0.941 |
| | | AWTV-BD | 37.82 | 10.51 | **0.976** |
| | | AEE-BD | **38.10** | **10.79** | **0.976** |
| | Gaussian | EP-$L_0$RG | 32.10 | 6.05 | 0.864 |
| | | AWTV-BD | 39.32 | 13.27 | 0.971 |
| | | AEE-BD | **39.50** | **13.45** | **0.972** |
| Dot | linear motion | EP-$L_0$RG | 27.58 | 11.22 | 0.953 |
| | | AWTV-BD | 28.75 | 12.39 | 0.970 |
| | | AEE-BD | **28.97** | **12.60** | **0.971** |
| | Gaussian | EP-$L_0$RG | 26.88 | 11.62 | 0.954 |
| | | AWTV-BD | 27.84 | 12.58 | 0.970 |
| | | AEE-BD | **28.00** | **12.74** | **0.971** |

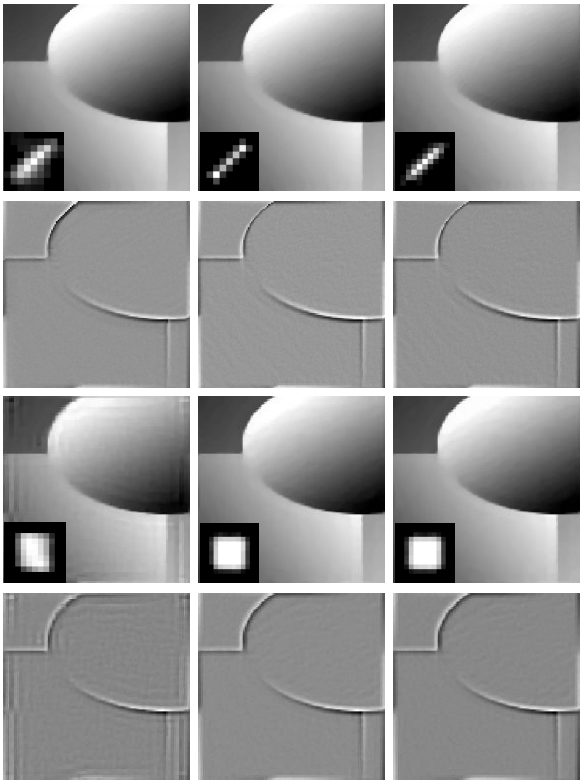

(a) EP-$L_0$RG (b) AWTV-BD (c) AEE-BD

**Fig. 3.** Blind deconvolution outcomes of different approaches for geometric images with the noise level of 0.005: linear motion blur (row 1, 2) and Gaussian blur (row 3, 4).

an adaptive weighted matrix, the localized regions recovered are more natural, especially the upper right spherical part of the Geometric image. From the residual images in Fig. 3, we observe that AEE-BD removes more noise and retains more image texture structure compared to AWTV-BD. This is owing to the fact that it is a higher-order model based on curvature information. From the recovered images in Fig. 4, it is clear that the results obtained by EP-$L_0$RG are very unsatisfactory, while the difference between the other two methods is not significant. Fortunately, the blur kernels restored by AEE-BD are closer to the original blur kernels compared to the results of AWTV-BD.

To further demonstrate the effectiveness of AEE-BD in blind image deconvolution, we give numerical and visual experimental results for adding 0.01 of high noise to blurred images. It's important to emphasize that the blur kernels applied to these test images are consistent with those used in the previous experiments. Table II displays the related numerical of results for the four test images obtained by the different methods. It reveals that AEE-BD continues to obtain the highest PSNR, ISNR, and SSIM values.

Figs. 5 and 6 show the recovered images, recovered blur kernels, and the locally enlarged images for the Satellite and Peppers images at a high noise level of 0.01, respectively. The enlarged images in Fig. 5 show that for each type of blur, the recovered image of EP-$L_0$RG is too smooth, resulting in the loss of many details. Furthermore, the recovered blur kernel is very different when compared to original kernel. In contrast, the blur kernel acquired from AEE-BD closely resembles the original kernel and has a better corrective effect. Meanwhile, it can be seen from the recovered images that the AEE-BD blind deconvolution results are better than the other two methods, especially since the black dot above the satellite body is closer to the clear image. From the

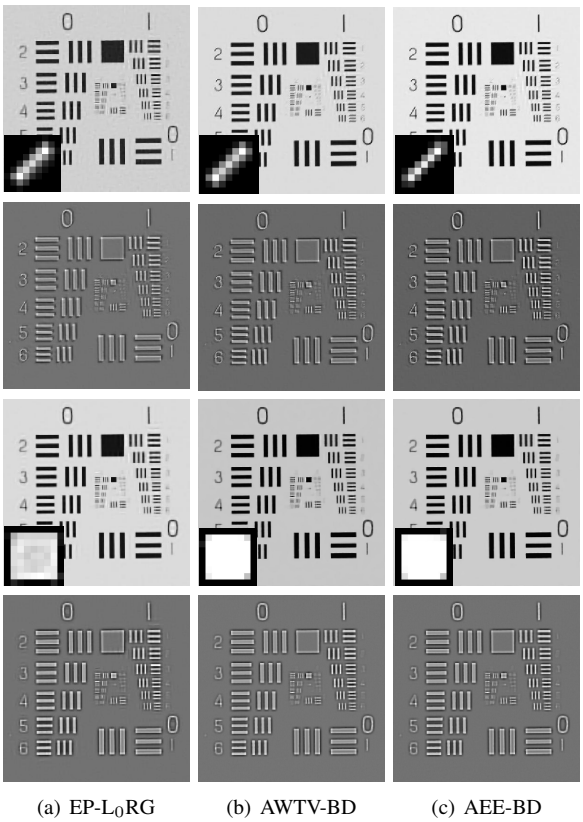

(a) EP-$L_0$RG (b) AWTV-BD (c) AEE-BD

**Fig. 4.** Blind deconvolution outcomes of different approaches for Dot images with the noise level of 0.005: linear motion blur (row 1, 2) and Gaussian blur (row 3, 4).

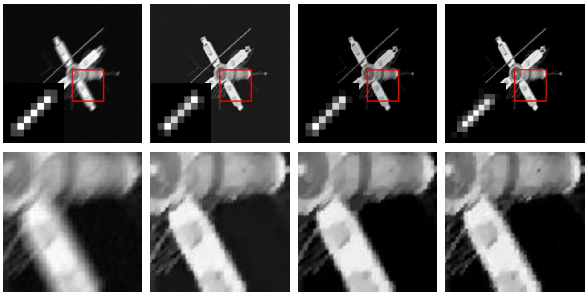

(a) linear motion (b) EP-$L_0$RG (c) AWTV-BD (d) AEE-BD

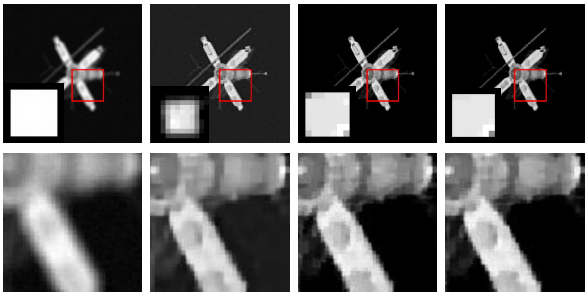

(e) Gaussian (f) EP-$L_0$RG (g) AWTV-BD (h) AEE-BD

**Fig. 5.** Results of blind deconvolution from different methods for Satellite image at a noise level 0.01.

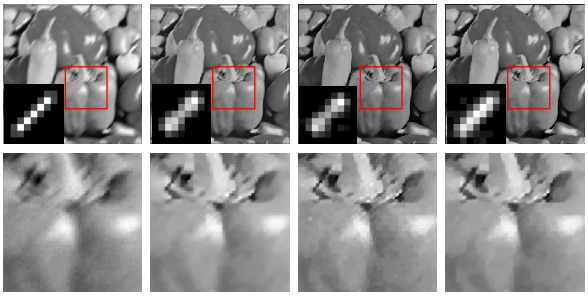

(a) linear motion (b) EP-$L_0$RG (c) AWTV-BD (d) AEE-BD

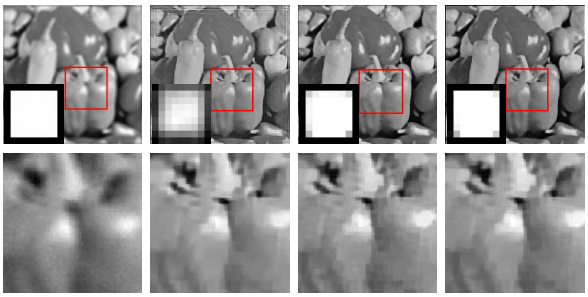

(e) Gaussian (f) EP-$L_0$RG (g) AWTV-BD (h) AEE-BD

**Fig. 6.** Results of blind deconvolution from different methods for Peppers image at a noise level 0.01.

**TABLE II** Blind deconvolution numerical results in Gaussian noise of 0.01 standardized variance.

| Image | Blur type | Method | PSNR | ISNR | SSIM |
|---|---|---|---|---|---|
| Satellite | linear motion | EP-$L_0$RG | 30.72 | 4.91 | 0.935 |
| | | AWTV-BD | 30.91 | 5.11 | 0.940 |
| | | AEE-BD | **31.26** | **5.45** | **0.953** |
| | Gaussian | EP-$L_0$RG | 27.47 | 3.37 | 0.852 |
| | | AWTV-BD | 28.82 | 4.82 | **0.900** |
| | | AEE-BD | **29.03** | **4.93** | 0.899 |
| Peppers | linear motion | EP-$L_0$RG | 26.84 | 3.46 | 0.879 |
| | | AWTV-BD | 29.11 | 5.73 | 0.892 |
| | | AEE-BD | **29.35** | **5.97** | **0.893** |
| | Gaussian | EP-$L_0$RG | 25.27 | 2.85 | 0.795 |
| | | AWTV-BD | 29.31 | 6.89 | 0.862 |
| | | AEE-BD | **29.47** | **7.05** | **0.867** |
| Geometric | linear motion | EP-$L_0$RG | 33.46 | 4.30 | 0.959 |
| | | AWTV-BD | 37.03 | 9.89 | **0.969** |
| | | AEE-BD | **37.21** | **10.05** | **0.969** |
| | Gaussian | EP-$L_0$RG | 31.43 | 5.47 | 0.861 |
| | | AWTV-BD | 37.97 | 12.00 | 0.958 |
| | | AEE-BD | **38.19** | **12.23** | **0.960** |
| Dot | linear motion | EP-$L_0$RG | 25.73 | 9.38 | 0.912 |
| | | AWTV-BD | 25.91 | 9.56 | 0.918 |
| | | AEE-BD | **26.16** | **9.81** | **0.929** |
| | Gaussian | EP-$L_0$RG | 26.27 | 11.02 | 0.917 |
| | | AWTV-BD | 26.49 | 11.25 | 0.954 |
| | | AEE-BD | **26.89** | **11.65** | **0.956** |

enlarged images of Peppers in Fig. 6, we easily see that AWTV-BD and AEE-BD outperform EP-$L_0$RG in preserving the image edges and local structure information, due to the fact that both of them employ the adaptive weighted matrix. However, AWTV-BD produces significant staircase effects in the smooth regions. With the application of curvature information, images restored by AEE-BD are more natural in flat regions.

## V. Conclusion

In this paper, we proposed a blind deconvolution model that utilizes the adaptive Euler's elastica regularization. Furthermore, we designed an efficient ADMM in this work, where the proposed model was split into several subproblems, each with a closed-form solution. The proposed model effectively restores the local features of the image while mitigating the presence of staircase effects, thereby achieving the desired deconvolution effect. Numerical experiments on both natural and synthetic images were conducted under two types of blur and two noise levels, showing that our method performs better than the previous two approaches. In the future, we will apply the presented adaptive technique to blind deconvolution of Poisson images. In addition, we will explore some acceleration technologies to reduce the computational cost.

## References

[1] G. Rioux, R. Choksi, T. Hoheisel, P. Marechal, and C. Scarvelis, "The Maximum Entropy on the Mean Method for Image Deblurring," *Inverse Problems*, vol. 37, no. 1, p. 015011, 2020.

[2] T. Adam and R. Paramesran, "Hybrid Non-convex Second-order Total Variation with Applications to Non-blind Image Deblurring," *Signal Image and Video Processing*, vol. 14, no. 1, pp. 115–123, 2020.

[3] J. Liu, R. Ma, X. Zeng, W. Liu, M. Wang, and H. Chen, "An Efficient Non-convex Total Variation Approach for Image Deblurring and Denoising," *Applied Mathematics and Computation*, vol. 397, p. 125977, 2021.

[4] W. Dong, K. Zhang, C. Zhu, G. Xu, F. Fei, and S. Tao, "Efficient Non-blind Deconvolution Method for Large Scale Blurred Image with Hybrid Regularizations," *Optik*, vol. 267, p. 169630, 2022.

[5] S. Xiao, "Image Restoration Algorithm Based on Double l0-Regularization and ALM," *Engineering Letters*, vol. 31, no. 1, pp. p52–65, 2023.

[6] R. Sukanesh, R. Harikumar, N. Balaji, and S. Balasubramaniam, "Analysis of Image Compression by Minimum Relative Entropy (MRE) and Restoration through Weighted Region Growing Techniques for Medical Images.," *Engineering Letters*, vol. 14, no. 1, pp. p84–89, 2007.

[7] S. Takahashi, M. Tanaka, and S. Ikeda, "Blind Deconvolution with Non-smooth Regularization via Bregman Proximal DCAs," *Signal Processing*, vol. 202, p. 108734, 2023.

[8] R. J. Fétick, L. Mugnier, T. Fusco, and B. Neichel, "Blind Deconvolution in Astronomy with Adaptive Optics: the Parametric Marginal Approach," *Monthly Notices of the Royal Astronomical Society*, vol. 496, no. 4, pp. 4209–4220, 2020.

[9] W. Z. Shao, J. Y. Li, W. W. Luo, M. L. Liu, and H. Deng, "A Geometric View to Reweighted Graph Total Variation Blind Deconvolution: Making It Faster and Better," in *Proc. IEEE 15th International Congress on Image and Signal Processing, BioMedical Engineering and Informatics*, 2022, pp. 1-5.

[10] J. Jia, "Single Image Motion Deblurring Using Transparency," in *Proc. IEEE Conference on Computer Vision and Pattern Recognition*, 2007, pp. 1-8.

[11] S. Cho and S. Lee, "Fast Motion Deblurring," in *Proc. IEEE ACM SIGGRAPH Asia 2009 Papers*, 2009, pp. 1-8.

[12] L. Sun, S. Cho, J. Wang, and J. Hays, "Edge-Based Blur Kernel Estimation Using Patch Priors," in *Proc. IEEE International Conference on Computational Photography*, 2013, pp. 1-8.

[13] S. H. Lim, Y. Wan, and U. Simsekli, "Chaotic Regularization and Heavy-Tailed Limits for Deterministic Gradient Descent," *Advances in Neural Information Processing Systems*, vol. 35, pp. 26590–26602, 2022.

[14] S. Xiao, "Blind Image Restoration Based on l1-l2 Blur Regularization," *Engineering Letters*, vol. 28, no. 1, pp. 148–154, 2020.

[15] J. Li and W. Lu, "Blind Image Motion Deblurring with $L_0$ Regularized Priors," *Journal of Visual Communication and Image Representation*, vol. 40, pp. 14–23, 2016.

[16] V. Papyan and M. Elad, "Multi-Scale Patch-Based Image Restoration," *IEEE Transactions on Image Processing*, vol. 25, no. 1, pp. 249–261, 2015.

[17] J. Pan, D. Sun, H. Pfister, and M. H. Yang, "Blind Image Deblurring Using Dark Channel Prior," in *Proc. IEEE Conference on Computer Vision and Pattern Recognition*, 2016 pp. 1628–1636.

[18] J. Dong, J. Pan, and Z. Su, "Blur Kernel Estimation via Salient Edges and Low Rank Prior for Blind Image Deblurring," *Signal Processing: Image Communication*, vol. 58, pp. 134–145, 2017.

[19] L. Chen, F. Fang, T. Wang, and G. Zhang, "Blind Image Deblurring with Local Maximum Gradient Prior," in *Proc. IEEE Conference on Computer Vision and Pattern Recognition*, 2019, pp.1742–1750.

[20] T. F. Chan and C. K. Wong, "Total Variation Blind Deconvolution," *IEEE Transactions on Image Processing*, vol. 7, no. 3, pp. 370–375, 1998.

[21] W. Li, Q. Li, W. Gong, and S. Tang, "Total Variation Blind Deconvolution Employing Split Bregman Iteration," *Journal of Visual Communication and Image Representation*, vol. 23, no. 3, pp. 409–417, 2012.

[22] I. El Mourabit, M. El Rhabi, and A. Hakim, "Blind Deconvolution Using Bilateral Total Variation Regularization: a Theoretical Study and Application," *Applicable Analysis*, vol. 101, no. 16, pp. 5660–5673, 2022.

[23] W. Shuai, H. Chunyuan, R. Huiqin, B. Hua, H. Jialin, and R. Changhui, "Multi-Frame Blind Deconvolution of Solar Images via Second-Order Total Generalized Variation," *Opto-Electronic Engineering*, vol. 50, no. 2, p. 220207, 2023.

[24] C. Xu, C. Zhang, M. Ma, and J. Zhang, "Blind Image Deconvolution via an Adaptive Weighted TV Regularization," *Journal of Intelligent Fuzzy Systems*, vol. 44, no. 4, pp. 6497–6511, 2023.

[25] Z. F. Pang, Y. M. Zhou, T. Wu, and D. J. Li, "Image Denoising via a New Anisotropic Total-Variation-Based Model," *Signal Processing: Image Communication*, vol. 74, pp. 140–152, 2019.

[26] Z. F. Pang, H. L. Zhang, S. Luo, and T. Zeng, "Image Denoising Based on the Adaptive Weighted $\mathrm{TV}^p$ Regularization," *Signal Processing*, vol. 167, p. 107325, 2020.

[27] M. Ma, C. Xu, J. Zhang, S. Wang, C. Deng, and Y. Wang, "Hyperspectral Sparse Unmixing Based on a Novel Adaptive Total Variation Regularization," *Infrared Physics and Technology*, vol. 127, p. 104362, 2022.

[28] J. Zhang, P. Li, J. Yang, M. Ma, and C. Deng, "Poisson Image Restoration Using a Novel Directional $\mathrm{TV}^p$ Regularization," *Signal Processing*, vol. 193, p. 108407, 2022.

[29] J. Yang, M. Ma, J. Zhang, and C. Wang, "Noise Removal Using an Adaptive Euler's Elastica-Based Model," *The Visual Computer*, vol. 38, pp. 1–12, 2022.

[30] J. Shen, S. H. Kang, and T. F. Chan, "Euler's Elastica and Curvature-Based Inpainting," *SIAM Journal on Applied Mathematics*, vol. 63, no. 2, pp. 564–592, 2003.

[31] H. Z. Chen, J. P. Song, and X. C. Tai, "A Dual Algorithm for Minimization of the LLT Model," *Advances in Computational Mathematics*, vol. 31, pp. 115–130, 2009.

[32] W. Zhu, X. C. Tai, and T. Chan, "Augmented Lagrangian Method for a Mean Curvature Based Image Denoising Model," *Inverse Problems and Imaging*, vol. 7, no. 4, pp. 1409–1432, 2013.

[33] M. Ma, J. Zhang, C. Deng, Z. Liu, and Y. Wang, "Adaptive Image Restoration via a Relaxed Regularization of Mean Curvature," *Mathematical Problems in Engineering*, vol. 2020, pp. 1–11, 2020.

[34] Q. Zhong, K. Yin, and Y. Duan, "Image Reconstruction by Minimizing Curvatures on Image Surface," *Journal of Mathematical Imaging and Vision*, vol. 63, pp. 30–55, 2021.

[35] X. C. Tai, J. Hahn, and G. J. Chung, "A Fast Algorithm for Euler's Elastica Model Using Augmented Lagrangian Method," *SIAM Journal on Imaging Sciences*, vol. 4, no. 1, pp. 313–344, 2011.

[36] J. Zhang, R. Chen, C. Deng, and S. Wang, "Fast Linearized Augmented Lagrangian Method for Euler's Elastica Model," *Numerical Mathematics: Theory, Methods and Applications*, vol. 10, no. 1, pp. 98–115, 2017.

[37] Y. Zhang, Y. Shi, L. Ma, J. Wu, L. Wang, and H. Hong, "Blind Natural Image Deblurring with Edge Preservation Based on $L0$ Regularized Gradient Prior," *Optik*, vol. 225, p. 165735, 2021.